Tonsil-derived mesenchymal stem cells incorporated in reactive oxygen species-releasing hydrogel promote bone formation by increasing the translocation of cell surface GRP78

Da Hyeon Choi [a,1], Kyeong Eun Lee [a,1], Se-Young Oh [b,c], Si Min Lee [d], Beom Soo Jo [e,f], Jue-Yeon Lee [f], Jong-Chul Park [g], Yoon Jeong Park [e,f,****], Ki Dong Park [d,***], Inho Jo [b,c,**], Yoon Shin Park [a,*]

[a] Department of Biological Sciences and Biotechnology, School of Biological Sciences, College of Natural Sciences, Chungbuk National University, Cheongju, 28644, Republic of Korea
[b] Department of Molecular Medicine, College of Medicine, Ewha Womans University, 25 Magokdong-ro-2-gil, Gangseo-gu, Seoul, 07804, Republic of Korea
[c] Graduate Program in System Health Science and Engineering, Ewha Womans University, 25 Magokdong-ro-2-gil, Gangseo-gu, Seoul, 07804, Republic of Korea
[d] Department of Molecular Science and Technology, Ajou University, 206, World cup-ro, Yeongtong-gu, Suwon-si, Gyeonggi-do, 16499, Republic of Korea
[e] Department of Dental Regenerative Bioengineering and Dental Research Institute, School of Dentistry, Seoul National University, Seoul, 03080, Republic of Korea
[f] Central Research Institute, Nano Intelligent Biomedical Engineering Corporation (NIBEC), #404 Biomaterial Research building, 101 Daehak-ro, Jongno-gu, Seoul, 03080, Republic of Korea
[g] Cellbiocontrol Laboratory, Department of Medical Engineering, Yonsei University College of Medicine, Seoul, 03722, Republic of Korea

ARTICLE INFO

ABSTRACT

Controlling the senescence of mesenchymal stem cells (MSCs) is essential for improving the efficacy of MSC-based therapies. Here, a model of MSC senescence was established by replicative subculture in tonsil-derived MSCs (TMSCs) using senescence-associated β-galactosidase, telomere-length related genes, stemness, and mitochondrial metabolism. Using transcriptomic and proteomic analyses, we identified glucose-regulated protein 78 (GRP78) as a unique MSC senescence marker. With increasing cell passage number, GRP78 gradually translocated from the cell surface and cytosol to the (peri)nuclear region of TMSCs. A gelatin-based hydrogel releasing a sustained, low level of reactive oxygen species (ROS-hydrogel) was used to improve TMSC quiescence and self-renewal. TMSCs expressing cell surface-specific GRP78 (csGRP78+), collected by magnetic sorting, showed better stem cell function and higher mitochondrial metabolism than unsorted cells. Implantation of csGRP78+ cells embedded in ROS-hydrogel in rats with calvarial defects resulted in increased bone regeneration. Thus, csGRP78 is a promising biomarker of senescent TMSCs, and the combined use of csGRP78+ cells and ROS-hydrogel improved the regenerative capacity of TMSCs by regulating GRP78 translocation.

1. Introduction

Mesenchymal stem cells (MSCs) are considered an essential tool in regenerative medicine owing to their multi-potency in various tissues. However, cellular senescence decreases MSC proliferation and differentiation potential, creating a bottleneck for clinical applications [1,2].

---

* Corresponding author. Department of Biological Sciences and Biotechnology, School of Biological Sciences, College of Natural Sciences, Chungbuk National University, Cheongju, 28644, Republic of Korea.
** Corresponding author. Department of Molecular Medicine, College of Medicine, Ewha Womans University, 25 Magokdong-ro-2-gil, Gangseo-gu, Seoul, 07804, Republic of Korea.
*** Corresponding author. Department of Molecular Science and Technology, Ajou University, 206, World cup-ro, Yeongtong-gu, Suwon-si, Gyeonggi-do, 16499, Republic of Korea.
**** Corresponding author. Department of Dental Regenerative Bioengineering and Dental Research Institute, School of Dentistry, Seoul National University, Seoul, 03080, Republic of Korea.
E-mail addresses: parkyj@snu.ac.kr (Y.J. Park), kdp@ajou.ac.kr (K.D. Park), inhojo@ewha.ac.kr (I. Jo), pys@cbnu.ac.kr (Y.S. Park).
[1] These authors contributed equally to this work.

Cellular senescence can be induced by two major factors: genetically programmed aging during developmental processes and endoplasmic reticulum (ER) stress [3–5]. Recent studies have focused on minimizing cellular senescence to improve the stemness and quality of MSCs to aid in their successful application in regenerative medicine [6,7].

TMSCs retain higher proliferation rate compared with BMSCs and ADMSCs, probably due to the fact that TMSCs are generally obtained from younger donors, average age of less than 10 years old. Most importantly, the unique surface markers and soluble mediators makes TMSCs as an attractive MSC candidate for practical and clinical implications due to their ease of obtaining, expanding as well as relatively low immunogenicity compared to MSCs of other sources. TMSCs have been tested in animal models of osteoporosis [8,9], osteoradionecrosis [10], or calvarial defect [11] and have demonstrated some promising outcomes as a feasible therapeutic treatment for bone-related disorders.

The events of cellular senescence associated with aging, such as telomere shortening, and neuroendocrine and immunological alterations, are spontaneous and inevitable. In contrast, ER stress-induced senescence can be prevented or reduced by controlling the extracellular environments [12]. ER stress results in the accumulation of somatic mutations and reactive oxygen species (ROS) production, eventually leading to cell damage and death. ROS production causes cellular exhaustion and increases cellular senescence and apoptosis in a dose-dependant manner [13]. Counterintuitively, ROS are essential for maintaining normal cellular processes [14,15]. Moreover, Jang and Sharkis (2007) reported that low ROS levels are crucial for hematopoietic stem cell precursors to maintain a quiescent state and self-renew [16]. Furthermore, an extremely low intracellular ROS level (below 0.001 µM) negatively impacts proliferation, differentiation, and immunity, suggesting that a low basal ROS level is essential for cellular physiology [15]. Since high ROS levels are toxic to cells, intracellular ROS levels are closely regulated to ensure that stem cells maintain tissue homeostasis and repair damaged tissues throughout the lifespan of an organism [13,17].

ROS are mainly produced via mitochondrial respiratory chain activity by the consumption of intracellular O_2 [18]; however, the ERs also play a role in generating ROS by way of Ca^{2+} leakage from the ER and oxidative stress [19,20]. During ER stress, the Ca^{2+} pool stored in the ER is released into the cytosol, thereby increasing the mitochondrial Ca^{2+} levels, altering the mitochondrial metabolism, and promoting ROS production [18,21,22]. In non-stressed cells, ROS are regulated by three unfolded protein response (UPR) sensor proteins - protein kinase R (PKR)-like endoplasmic reticulum kinase, PERK; inositol-requiring enzyme 1, IRE1; and activating transcription factor 6, ATF6 - embedded in the ER membrane. Glucose-regulated protein 78 (GRP78) binds to these three UPR sensors but remains inactive until required [17,23].

GRP78 is an ER chaperone protein, also known as "BiP" or "HSPA5". It is a member of the heat shock protein 70 superfamily and acts by regulating ER stress sensors' activities to sustain ER protein-folding, thereby maintaining a balance between cell viability and apoptosis [24]. Although GRP78 is traditionally thought to reside exclusively in the ER lumen, it can also be secreted and actively translocated to other cellular locations, including the cell surface, cytosol, nucleus, and mitochondria, to regulate cell signaling, proliferation, invasion, apoptosis, inflammation, and immunity [24–26]. Notably, cell surface-specific GRP78 (csGRP78), localized in the plasma membrane, exerts a receptor-like function, and increases proliferation, motility, and survival [22,24,27]. Although no direct evidence has shown that csGRP78 regulates stem cell function and senescence, the loss of GRP78 is reportedly associated with aging and age-related diseases [28], indicating a potential link with age-related MSC senescence.

To create an optimal microenvironment for MSCs to proliferate and differentiate effectively while minimizing cellular senescence, we previously developed gelatin-based (H_2O_2)-releasing hydrogels. The hydrogel provides an artificial cellular microenvironment by releasing 50–250 µM of ROS to support the 3D cell culture growth of human dermal fibroblasts without compromising on cytocompatibility [29]. Here, we modified the stiffness and glucose oxidase (GOx) concentration of the hydrogel to obtain a sustained release of low levels of ROS. We investigated the potential effects of the ROS-hydrogel in minimizing the impacts associated with cellular senescence of tonsil-derived MSCs (TMSCs) and validated its potential application as a novel material for improving the efficacy of MSC-based regenerative therapies.

2. Materials and methods

2.1. TMSCs

Isolation and experimental groups Isolation of TMSCs was conducted in accordance with aa previously described protocol, with a slight modification [30]. For the detailed isolation methods, please refer to the Supplementary Information. TMSCs were subcultured on individual 100 mm² dishes, and the cells at 80% confluence were detached using 0.25% trypsin-EDTA (Gibco) for 3 min. This step was repeated until 20 to 25 passages were reached, to induce replicative senescence in TMSCs. The maximum number of passages was set based on the decreased proliferation capacity. In this study, TMSCs were categorized into two groups: control TMSCs (Ctrl; passages 5–8) and culture aged TMSCs (CA; passages 20–25). The doubling time of TMSCs with each passage number was calculated using the Patterson formula: doubling time, (h) = [{(T − T_0)(log2)}/(logN − $logN_0$)] T is time (h), and N is the cell count.

2.2. Senescence-associated β-galactosidase assay

As the serial passage progressed, the morphological changes in TMSCs were observed with an inverted microscope (Olympus) to observe senescent TMSCs. Senescent TMSCs were identified by staining the cells with senescence-associated β-galactosidase (SA-β-gal) using an SA-β-gal staining kit (Cell Signaling Technology), according to the manufacturer's instructions. For the detailed procedure, please refer to Supplementary Information.

2.3. Subcellular fractionation of TMSCs and Western blot analysis

After harvesting the subcultured TMSCs at different passage numbers, the cells were washed thrice with ice-cold PBS. Subcellular fractionation was performed using a subcellular protein fractionation kit, according to the manufacturer's instructions (Thermo Fisher). Intracellular fractions were extracted using a suitable buffer and by centrifugation of each subcellular fraction. The collected subcellular fractions were then used for Western blot analyses to determine the protein levels. For detailed description on the Western blot analysis protocol, please refer the Supporting Information.

2.4. FACS analysis

Control or CA TMSCs (1.0 × 10⁵ cells) were incubated with fluorescein isothiocyanate (FITC)- or phycoerythrin (PE)-conjugated monoclonal antibodies targeting Isotype-PE, Isotype-FITC, CD14, CD34, CD45, CD73, CD90, and CD105 (BD Biosciences), for 30 min at 4 °C. The cell populations were analyzed using a FACScan instrument (FACSCalibur-S System; BD Biosciences), and the data obtained were analyzed using the FlowJo software (BD Biosciences).

2.5. Cell cycle analysis

Cell cycle stage was examined by measuring the DNA content of nuclei labeled with propidium iodide (PI, Abcam). For the cell cycle analysis, either the control or the CA TMSCs (1 × 10⁵ cells) were harvested by trypsinization and gently pelleted by centrifugation at $300 \times g$ for 5 min. The pellets were washed and resuspended in 200 µl DPBS. The

resuspended cells were transferred drop-wise into 70% ethanol (800 μl) and fixed for 1 week. The cells fixed in ethanol were collected, washed, and resuspended in PI staining solution (50 mg/ml) containing RNase A (100 mg/ml), and incubated in the dark for 30 min at room temperature. A FACScan (FACSCalibur-S) was used to analyze the cell cycle, and the FlowJo software was used for data analysis.

2.6. Measurement of metabolic changes

TMSCs were seeded in a 60 mm^2 culture dish. When the cells reached confluence, they were washed thrice with DPBS. To determine the oxygen consumption rate (OCR), 1.2×10^4 cells were resuspended in 1 ml of fresh warm DMEM supplemented with 10% FBS and 2 mM glutamine. The cells were left to respire for 10 min to monitor the basal oxygen consumption. Subsequently, 1.25 μM oligomycin, 1 μM carbonlcyanide 4-(trifluoromethoxy)-phenylhydrazone (FCCP), and 0.5 μM rotenone/antimycin A (R/A) were added to determine the sources and contribution of mitochondrial and/or non-mitochondrial oxygen consumption. Real-time OCR was monitored using a Seahorse analyzer XF96 (Agilent).

2.7. Transcriptomic and proteomic analysis

For detailed information on the transcriptomic and proteomic analyses performed, please refer the Supporting Information.

2.8. Immunofluorescence staining of cell membranes

To perform the immunofluorescence assay, TMSCs were fixed with 4% PFA and washed thrice with PBS. The cell membranes of the fixed TMSCs were permeabilized for 10 min at room temperature using 0.5% Triton X-100 and rinsed with PBS. After permeabilization, the non-specific binding sites were blocked with blocking buffer, composed of PBS supplemented with 3% bovine serum albumin, for 1 h. Next, the cells were incubated overnight with specific primary antibodies against GRP78 (1: 500 dilution; Abcam) followed by incubation with blocking buffer. The cells tagged with GRP78 antibodies were washed with PBS and incubated with goat anti-rabbit secondary antibodies conjugated with FITC (1: 500 dilution) for 1 h in a humid and dark chamber. The nuclei were counterstained with DAPI for 3 min. The cells were observed and imaged under a confocal microscope (LSM-880 with Airyscan, ZEISS).

2.9. MACS

The magnetic beads for the MACS column were incubated in a binding buffer containing primary GRP78 and secondary goat anti-rabbit antibody complexes for 12 h. The magnetic beads were washed thrice with PBS and loaded onto a MACS separation column fitted with a magnet (MiniMACs; Miltenyi Biotec). The binding buffer was run through the column once. Subsequently, the heterogeneous pool of TMSCs in the binding buffer were loaded to run through the separation column. The unbound cells were collected through the column and designated as "csGRP78- cells" The remaining bound TMSCs were released from the column by running an elution buffer through the column. The collected cells were designated as "csGRP78+ cells".

2.10. GRP78 knockdown experiments using siRNA GRP78

Protein expression in csGRP78+ cells was knocked down using siRNA. Two days prior to the transfection, the MACS sorted csGRP78+ cells were grown in 6-well plates containing DMEM supplemented with 10% FBS. GRP78 siRNA and scrambled siRNA were purchased from Santa Cruz Biotechnology (Santa Cruz). The scrambled control siRNA or GRP78 siRNA was transfected into csGRP78+ cells using Lipofect-amine2000 and LipoPLUS (Thermo Fisher). After the transfection, the cell lysates were collected and analyzed using Western blot analysis.

2.11. Synthesis and physicochemical characteristics of the ROS-hydrogel

The ROS-hydrogel was fabricated by mixing two types of solutions (sol A and sol B). To prepare solution A, HRP (0.025 mg/ml) and GOx (0 − 10 μU/ml) were dissolved in DPBS, followed by mixing with 2.5 wt% GH solution (volume ratio of GH/HRP/GOx = 8:1:1). To prepare solution B, 2.5 wt% GH was dissolved in H_2O_2 (0.035 − 0.13 wt%) and glucose (500 mM) (volume ratio GH/H_2O_2/glucose = 8:1:1). The solutions A and B were gently mixed in a volume ratio of 1:1 and shaken at room temperature in a 6-well plate for 2 min with a yellow tip to create the ROS-hydrogel. The elastic modulus (G) and viscous modulus (G′) of the hydrogels were measured using a rheometer (Advanced Rheometer GEM-150-050, Bohlin Instruments, USA), in oscillation mode, with a frequency of 0.1 Hz and a strain of 0.01% using parallel plate geometry (diameter = 25 mm, gap = 0.5 mm). To explore the effect of crosslinking density on the elastic modulus, 0.035–0.13 wt% H_2O_2 was used to fabricate the hydrogels.

2.12. Measurement of cumulative H_2O_2 release from the ROS-hydrogels

To measure the amount of H_2O_2 released from the ROS-releasing GH hydrogels, a quantitative peroxide assay kit (Pierce) using the ferrous ion (Fe^{2+}) oxidation xylenol orange assay was used. Briefly, 100 μl of ROS-releasing GH hydrogels, including GOx 0, 5, and 10 μU/ml (GOx0, GOx5, and GOx10, respectively) were prepared in a 48-well plate and incubated with 900 μl DPBS. We collected media at pre-determined time points, and the same amount of fresh medium was added to maintain a constant total volume of media throughout the experiment. Ten micro-liters each, of the collected media, were added to a 96-well plate, to which 100 μl of the assay kit solution was added using a multichannel pipette. The reaction was allowed to progress for 20 min at room temperature. Subsequently, the absorbance was measured at 595 nm using a microplate reader (BioTek).

2.13. Establishment of a critical calvarial defect

All animal experiments and surgical procedures were approved by the Institutional Animal Care and Use Committee of Chungbuk National University (IACUC ID: CBNUA-136R-19-01). Male Sprague Dawley rats (7 weeks old, 350 g) were supplied by Samtako Biokorea Inc. (Osan, Korea). Before surgery, rats received a subcutaneous injection of zoletil (20 μg/kg) to produce an anesthetic effect. Under sterile conditions, a sagittal incision was made from the orbital ridge for a distance of 10 mm. Skin flaps on either side were retracted to expose the calvaria. A hand-held drill fitted with a stainless-steel trephine drill bit was used at high speed to create a full-thickness 8 mm-diameter calvarial defect on the skull bone of each rat. Sterile PBS was used for irrigation during drilling. All hydrogel implants with or without GRP78+ TMSCs were placed in the calvarial defect area. Soft tissue compartments were closed with 4–0 Vicryl fiber, and skin incisions were closed using Prolene 5–0 nylon interrupted sutures. The animals were monitored every hour after the surgery. Post-surgery, buprenorphine was used to minimize pain or discomfort, and all rats were monitored for signs of infection. At the end of 4 weeks, the rats were euthanized using CO_2, and the calvarial bone tissues were collected for further experiments.

2.14. Micro-computed tomography imaging and histological analysis

Micro-CT images were obtained to monitor osteogenesis progression at the calvarial defect site using Quantum FX micro-CT (PerkinElmer), with the following parameters: 90 kVand 160 μA, and a field of view of 24 mm. The images were analyzed using the CTAn software (Bruker). The skull samples containing defective sites were retrieved, fixed in formalin, decalcified, paraffin-embedded, and subjected to H&E staining and Masson's trichrome staining.

2.15. Statistical analysis

All values are presented as the mean ± standard deviation (S.D.). All graphs in this manuscript were generated using the GraphPad Prism 7 software (GraphPad Software). Statistical significance was analyzed using the Student's t-test or one-way analysis of variance (ANOVA), followed by the Tukey's post hoc multiple comparison test. Significant differences among experimental groups are indicated using different alphabets, and the level of significance is denoted as $* p < 0.05$, $** p < 0.01$, and $*** p < 0.001$.
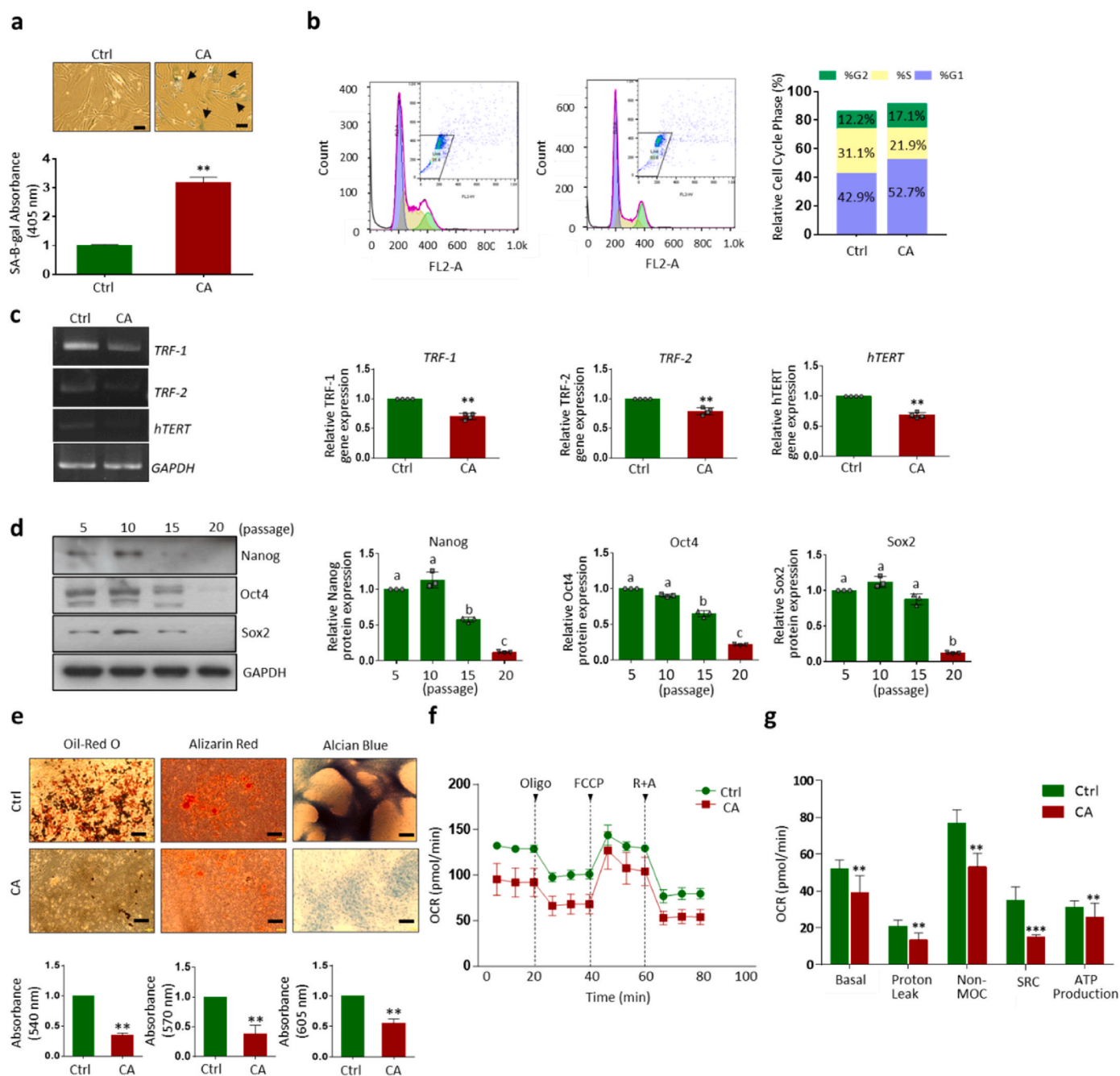

Fig. 1. Characteristics of control (Ctrl) and culture-aged (CA) TMSCs. a) Senescence-associated β-galactosidase (SA-β-gal)-stained TMSCs in the two experimental groups. Black arrows indicate blue-colored SA-β-gal-stained cells (Magnification: × 200; scale bar = 200 μm). The absorbance of SA-β-gal-stained samples was measured at 405 nm. b) The TMSCs from each experimental group were stained with PI staining solution, and flow cytometry was used to analyze the stage of cell cycle. c) Relative changes in the expression of *TRF-1*, *TRF-2*, and *hTERT* in the two experimental groups. d) Relative changes in the protein expression of the embryonic stem cell markers Nanog, Oct4, and Sox2 in the experimental groups, quantified using Western blot analyses. e) Mesodermal differentiation potentials of Ctrl and CA TMSCs indicated by the optical density of extracts from the cells stained with Oil Red O (adipogenesis), Alizarin Red S (osteogenesis), and Alcian Blue (chondrogenesis) solutions, determined at their respective characteristic absorbance. f) Mitochondrial activity of Ctrl and CA groups was determined by examining the cellular oxygen consumption rates (OCRs). g) Maximal respiration rate (pmol/min), ATP production (based on respiration), basal level of respiration (pmol/min), proton leak, non-mitochondrial oxygen consumption (non-MOC), spare respiratory capacity (SRC), and ATP production during oxidative phosphorylation in mitochondria were determined in the Ctrl and CA groups. Statistical significance is denoted as $p < 0.01$ (**), and $p < 0.001$ (***) (n = 3), and the alphabets in the figure indicate the significant differences among the experimental groups ($p < 0.05$). (For interpretation of the references to color in this figure legend, the reader is referred to the Web version of this article.)

3. Results

3.1. Development of culture-aged (CA) senescence model of TMSCs

Senescence-associated β-galactosidase (SA-β-gal) staining revealed that the CA TMSCs group had a 3.2 ± 0.2-fold higher number of X-gal-positive cells compared to the control group (Fig. 1a) ($p < 0.01$). Morphological changes, including cell length and width, were measured in the cultured TMSCs (Fig. S1a). Compared to control TMSCs, CA TMSCs were significantly enlarged (246.2 ± 36.5 vs. 182.9 ± 33.3 μm) and flattened (28.6 ± 9.0 vs. 21.3 ± 6.9 μm). Additionally, we found that replicative senescence affected the cell cycle, decreasing the S phase
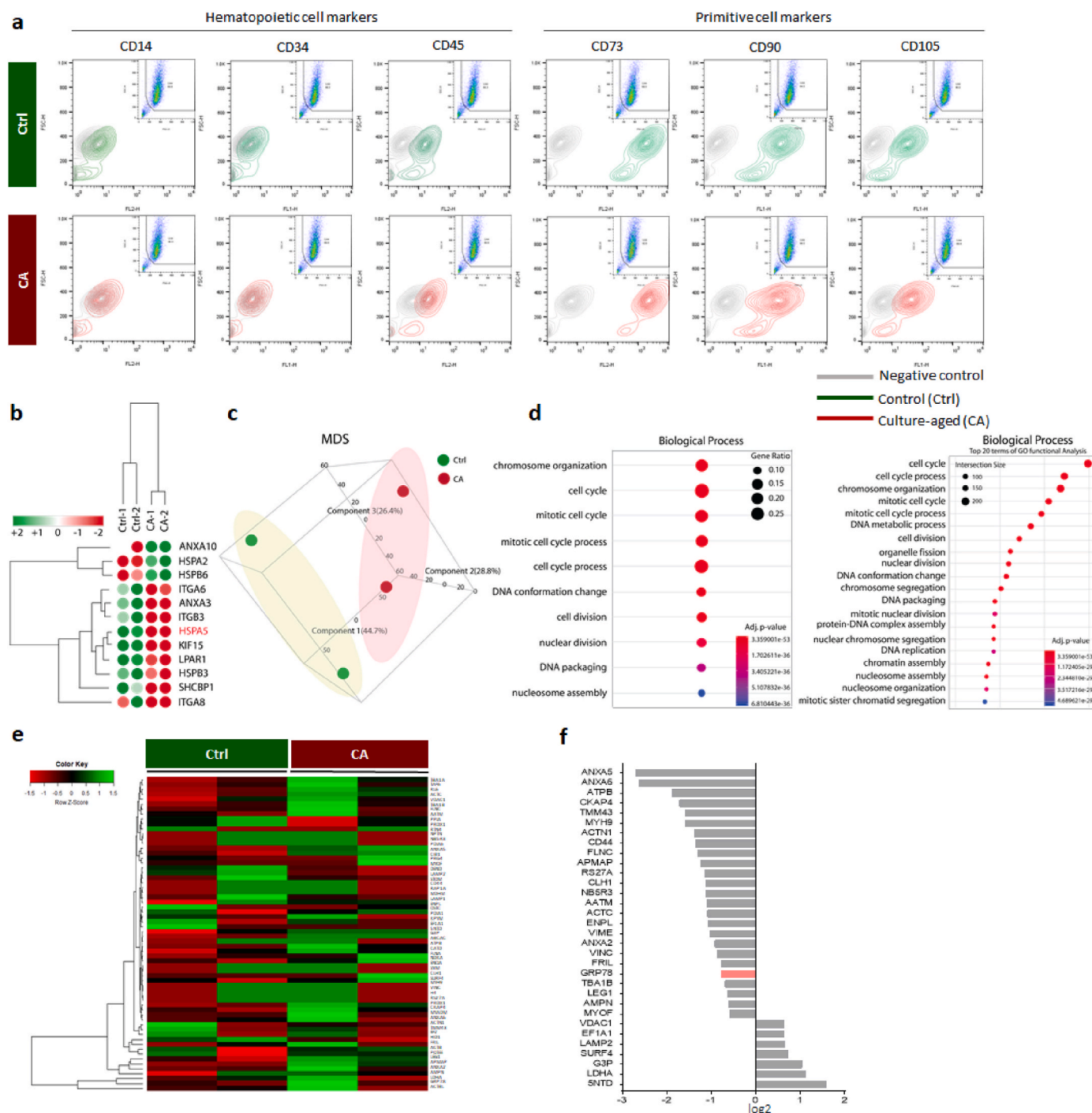

Fig. 2. The expression of cell surface markers and transcriptomic and proteomic profiles of control (Ctrl) and culture-aged (CA) TMSC groups. a) Hematopoietic (CD14, CD34, and CD45) and primitive (CD90, CD73, and CD105) surface markers of TMSCs were analyzed using FACS. Marker protein expression in Ctrl and CA TMSCs is marked using green and red circles, respectively. Gray circle indicates negative control. b) A partial heatmap of hierarchical clustering analysis indicates the differentially expressed genes (rows) among the control and CA TMSCs. c) Comparison of the MDS plots of microarray gene expression data of control and CA TMSCs. d) The distribution of GO terms for the DEGs among control and CA TMSCs were annotated according to the ontology categories, which included the top 20 enrichment genes. e) Heat map analyses of the correlation between all proteins determined by proteomic analysis and the cluster identified by similar feature analysis. f) The significantly upregulated or downregulated proteins of Ctrl and CA groups are presented as log₂ fold-change. (For interpretation of the references to color in this figure legend, the reader is referred to the Web version of this article.)

from 31.1 to 21.9%, while increasing the relative percentages of cells in the G1 and G2 phases from 42.9 to 52.7% and 12.2 to 17.1%, respectively (Fig. 1b). Furthermore, the doubling time of the TMSCs gradually increased with increase in the passage number; the average doubling time below passage 15 (the control TMSCs) was 40.1 ± 1.8 h, whereas the doubling time from passage 20 to 25 exceeded 45 h (Fig. S1b).

RT-PCR analyses showed that compared to the control, the CA TMSCs had significantly lower expression of senescence-related genes; for instance, the expression of telomere regulation factor (TRF)-1, TRF-2, and human telomerase reverse transcriptase (hTERT) in the CA TMSCs was 0.6 ± 0.1-, 0.8 ± 0.1-, and 0.7 ± 0.1-fold lower than that in the control TMSCs (Fig. 1c), respectively. The protein expression of MSC stemness markers, Nanog, Oct4, and Sox2, began to decline after passage 10 until passage 20 (Fig. 1d).

Furthermore, we investigated the effects of replicative senescence on the multi-differentiation potential of TMSCs, such as adipogenesis, osteogenesis, and chondrogenesis (Fig. 1e). Compared to control TMSCs, CA TMSCs showed significantly reduced mesodermal differentiation potentials, which was evident from the significantly decreased lipid droplet formation (0.4 ± 0.1-fold, $p < 0.01$), mineralization (0.4 ± 0.1-fold, $p < 0.01$), and proteoglycan aggrecan levels (0.5 ± 0.1-fold, $p < 0.01$). To determine the effect of replicative senescence on the migration of the control and CA TMSCs, these cells were applied to the cell tracking system and monitored for 24 h in a CO_2 chamber (Supplementary Fig. 1c), following which the migration speed of CA TMSCs (17.8 ± 5.8 μm/h) was reduced by 26.0% compared to control TMSCs (13.2 ± 4.9 μm/h).

The cellular oxygen consumption rate (OCR) in mitochondria was investigated as an index of oxidative and cellular metabolic changes caused by replicative senescence. The OCRs from the different components were calculated (Fig. 1f). As shown in Fig. 1f, cultured TMSCs exhibited a lower OCR compared to the control. The CA TMSCs showed significantly reduced basal respiration, proton leak, non-mitochondrial respiration, and ATP production compared to the control ($p < 0.01$). Sequential injection of the indicated inhibitors (Oligo, FCCP, and R + A) was used to calculate the spare respiratory capacity (SRC, Fig. 1g) and ATP production. The cell-specific basal mitochondrial stress levels, which are often used as indicators of metabolic rate (52.7 ± 4.7 to 39.2 ± 9.1 pmol/min; $p < 0.01$), proton leak (20.9 ± 3.3 to 13.4 ± 3.8 pmol/min; $p < 0.01$), non-mitochondrial oxygen consumption (non-MOC, 76.9 ± 7.1 to 53.1 ± 7.3 pmol/min; $p < 0.01$), SRC (15.1 ± 12.2 to 35.0 ± 7.2 pmol/min; $p < 0.001$), and ATP production (31.2 ± 3.4 to 25.8 ± 7.5 pmol/min; $p < 0.01$) were significantly decreased in the control compared to the CA group.

3.2. Immunophenotypic and quantitative transcriptomic and proteomic characterization of TMSCs

The immunophenotypic differences between the two groups, the control and CA TMSCs, were investigated using flow cytometry. Both TMSC groups exhibited strong expression of the primitive cell markers CD73, CD90, and CD105, but weak expression of the hematopoietic lineage markers CD14, CD34, and CD45 (Fig. 2a). There were no significant differences in the levels of these markers between the control and CA groups, indicating that these markers may not be suitable markers for identifying TMSCs with replicative senescence.

To identify representative senescence markers to selectively isolate senescent TMSCs from a heterogeneous pool of TMSCs, we conducted transcriptomic and proteomic studies to analyze the differentially expressed proteins between the control and CA TMSCs (Fig. 2b-f, Tables S1 and 2). Transcriptomic data from previous studies were further reanalyzed, validating GRP78 as a representative marker associated with the replicative senescence of TMSCs (Tables S1 and 2) [30]. In the partial heatmap distribution, transcriptomic differences between control and CA TMSCs were presented as a $\log_2$-fold change (Fig. 2b). Based on multidimensional scaling (MDS) scores, the CA TMSCs were

distinguished from the control (Fig. 2c). The genes from control and CA TMSCs were categorized as highly differentially expressed genes according to the Gene Ontology (GO) classification of biological processes, which included the top 20 enriched terms (Fig. 2d). The transcriptomic GO results are presented in Supplementary Tables 1 and 2 Most transcriptomic data can be found in the GEO accession number, GES149588.

We compared the changes in protein abundance in each group. Heat map analysis of the correlated proteins obtained by proteomic and cluster analyses is shown in Fig. 2e. Proteomic analyses showed changes in the exponentially modified protein abundance index (emPAI) values between the two groups (Fig. 2f, Table S3). For numerical comparison, a fold difference higher than 1.5 in protein levels was considered a significant change. The expression of 25 proteins in the CA TMSCs decreased, while that of 7 proteins increased, compared to the control TMSCs. Most of the identified proteins belonged to the cytoskeletal and extracellular matrix-related protein families (Fig. 2f). Transcriptomic analyses showed that *HSPA5* expression was significantly decreased in CA TMSCs, as confirmed by proteomic analyses (Fig. S2a). The GRP78-centered regulatory networks were significantly associated with senescence-related proteins, including cytoskeletal proteins (ACTN1, TUBA1A, and TUBA1B) and proteins related to proliferation regulation (ENO1, PH4B, and EEF2, Fig. S2b). Therefore, we selected GRP78 as a representative senescence marker to isolate senescent TMSCs from a heterogeneous TMSC pool. The proteins identified by proteomic analyses were classified according to their subcellular location, such as Golgi, cytoplasm, secreted protein, mitochondria, nucleus, ER membrane, cell membrane, lysosome, and other fractions (Fig. S2c). Of these, the protein levels in the mitochondria, nucleus, ER membrane, and cell membrane fraction of the CA group showed a considerable increase compared to that in the control group.

3.3. Changes in gene and protein expression patterns of GRP78 with senescence

As the replicative senescence of TMSCs progressed, the gene (Fig. 3a) and protein (Fig. 3b) expression of GRP78 significantly decreased, especially after passage 10 and 20, both of which had 0.3 ± 0.1-fold lower GRP78 protein expression compared to the TMSCs at passage 5 ($p < 0.001$). This was further validated with adipose tissue-derived MSCs (AD-MSCs), and a significant decrease in GRP78 expression was observed in the AD-MSCs at passages 10 and 20 (CA) compared to that of AD-MSCs at passage 5 (control) (Figs. S3a and b). We further examined whether GRP78 levels decreased with increasing passage numbers in other non-MSC types, such as PANC-1 (pancreatic cancer cells) and NIH3T3 fibroblast cell lines. As shown in Figs. S3c and d, there were no significant changes in GRP78 levels between cells at different passages, implying that the changes in GRP78 levels are likely to be MSC-specific phenotypes observed in TMSCs with replicative senescence.

To find a link between GRP78 regulation and ER stress, we examined the changes in ATF6, phosphorylated ATF6^{Thr166}, IRE1α, and PERK levels using Western blot analysis (Fig. 3c). The protein levels of ATF6 and PERK were significantly decreased in TMSCs at passage 20, while p-ATF6^{Thr166} level was dramatically decreased after passage 15. In contrast, the level of IRE1α was unaffected by the passage number. To determine the changes in GRP78 localization with senescence, we analyzed GRP78 expression in different subfractions of the control and CA TMSCs (Fig. 3d). Compared to the control TMSCs, the CA TMSCs had a significantly decreased GRP78 expressions in cytosolic (0.4 ± 0.1-fold) and membranous (0.3 ± 0.1-fold) fractions compared to that of control TMSCs. While GRP78 expression in the nuclear fraction showed significantly increased expression in CA TMSCs (3.4 ± 0.1-fold) compared to the control TMSCs, which is the opposite expression pattern or even more dramatic difference than other two cellular fractions in cytoplasm and membrane (Fig. 3d). Based on these results, GRP78 expressed in the cell membrane was chosen as a reliable selection marker for distinguishing young and senescent cell populations in a heterogeneous
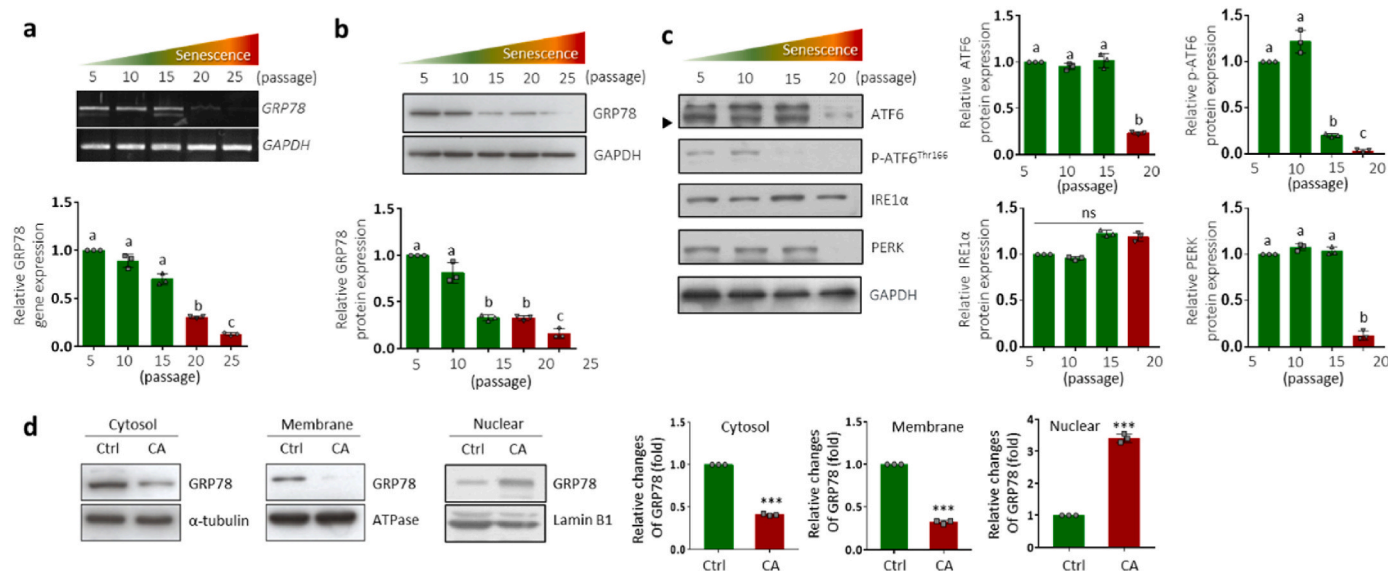
Fig. 3. Expression of genes and proteins involved in the GRP78-related signaling pathway in TMSCs at different passages. a, b) Gene and protein expression profile of GRP78 in TMSCs at passage 5, 10, 15, 20, and 25. c) Protein expression profile of representative ER stress markers: ATF6, p-ATF6^{Thr166}, IRE1, and PERK. d) Protein expression profiles of GRP78 in cell fractions, including cytosol, cell membrane, and nucleus, of control (Ctrl) and culture-aged (CA) TMSC groups were examined and compared. All bar graphs represent the fold changes normalized with each of the reference proteins. Statistical significance is denoted as $p < 0.001$ (***) (n = 3), and the alphabets in the figure indicate the significant differences among the experimental groups ($p < 0.05$).

pool of TMSCs.

3.4. Translocation of GRP78 with senescence in TMSCs

We labeled GRP78 with GFP to investigate the effect of replicative senescence on the intracellular localization of GRP78 in the control and CA TMSCs. In control TMSCs, GRP78 was evenly distributed in the cytoplasm and cell membrane until passage 10, but in the CA TMSCs, GRP78 was mainly localized around the perinuclear region at passage 15 and predominantly accumulated in the nucleus by passage 20 (Fig. 4a and b). These findings indicate that, with the induction of replicative senescence in TMSCs, GRP78 gradually translocates from the cytoplasm to the nucleus. Thus, changes in the expression and distribution of intracellular GRP78 is a hallmark of replicative senescence in MSCs.

3.5. Efficacy of sorted csGRP78+ TMSCs

TMSCs at low passage numbers retain GRP78 in the cytosol and cell membrane, and replicative senescence induces the localization of GRP78 to the nucleus, suggesting that GRP78 expressed on the cell membrane of TMSCs can be a marker for sorting cells with greater stem cell potential. Therefore, we used magnetic-activated cell sorting (MACS), as illustrated in Fig. 5a, to isolate GRP78-positive (csGRP78+) cells. We confirmed the efficacy of MACS for sorting GRP78+ cells using fluorescence-activated cell sorting (FACS) analysis and compared the number of csGRP78+ cells in the control and CA TMSC pools (Fig. S4a). We also examined the difference in the intracellular distribution of GRP78 between csGRP78+ and csGRP78- cells using an immunofluorescence assay (Fig. S4b). In csGRP78+ cells, GRP78 was expressed in the cell membrane and cytoplasmic regions, while in csGRP78- cells, GRP78 was primarily expressed in the (peri)nuclear region. Additionally, comparison of GRP78 expression in csGRP78+ and csGRP78-
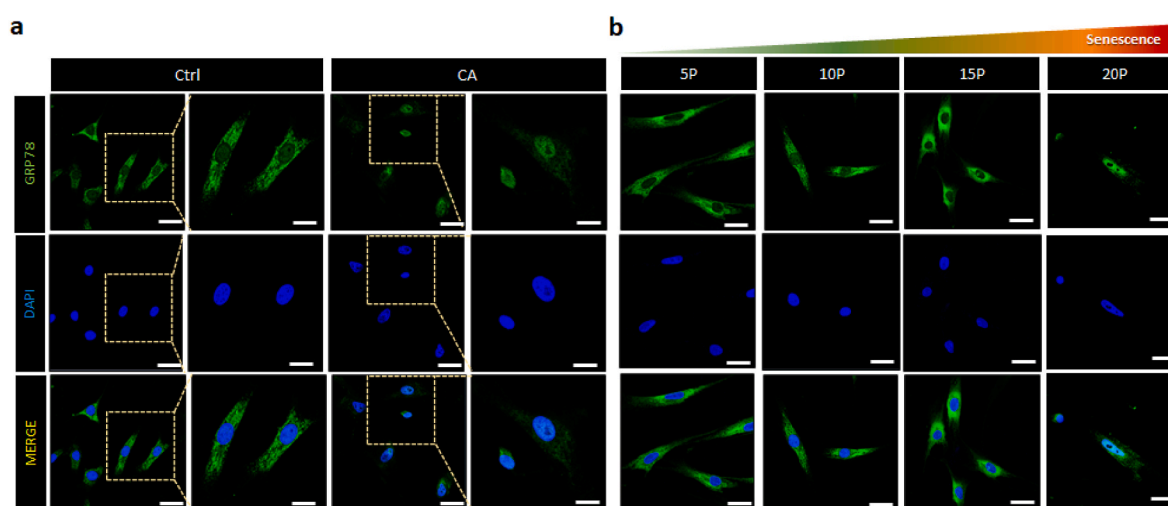

Fig. 4. Intracellular distribution of GRP78. Intracellular distribution of GRP78 in a) control (Ctrl) and b) culture-aged (CA) TMSCs at passage 5, 10, 15, and 20 (scale bar = 20 μm, n = 3).
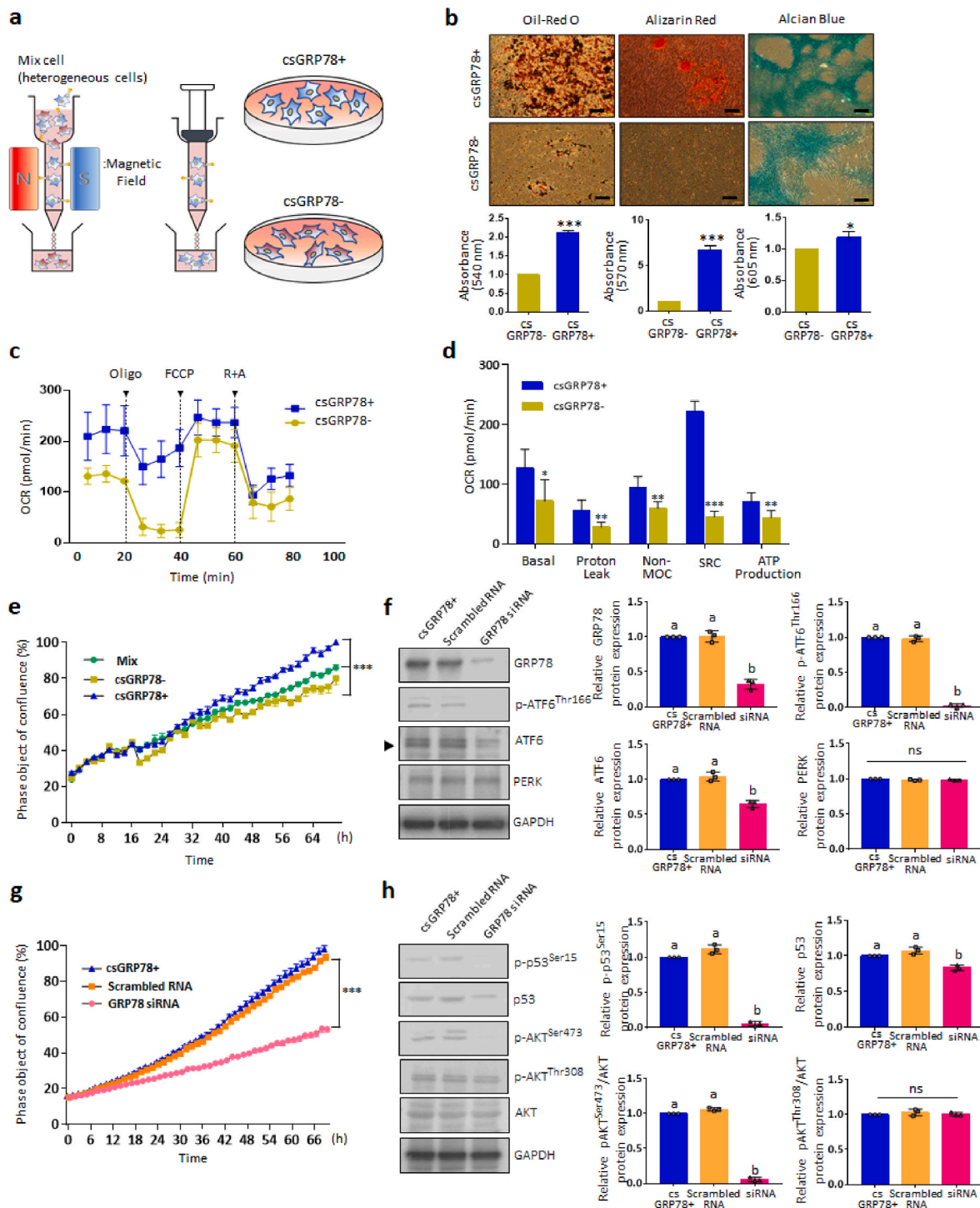
Fig. 5. Isolation of csGRP78+ cells by MACS. a) Schematic illustration of the use of MACS to separate the csGRP78+ and csGRP78- cells from a mixed TMSC population. b) Mesodermal differentiation potentials of csGRP78+ and csGRP78- cells (Scale bar = 400 μm). c, d) Mitochondrial activity, basal OGC, proton leak, non-MOC, SRC, and ATP production in csGRP78+ and csGRP78- cells. e) Cell proliferation profile of csGRP78+ *vs.* csGRP78- cells, and g) csGRP78+ *vs.* csGRP78+ cells transfected with GRP78 siRNA. f) Western blot analyses of GRP78, ER stress markers, and h) molecules involved in p53 and AKT signaling pathways in csGRP78+ cells transfected with GRP78 siRNA. Statistical significance is denoted as $p < 0.05$ (*), $p < 0.01$ (**), and $p < 0.001$ (***) (n = 3). and the alphabets in the figure indicate the significant differences among the experimental groups ($p < 0.05$).

TMSCs at each passage (Fig. S4c) revealed that unsorted control TMSCs mainly comprise csGRP78+ cells, while csGRP78- cells form the major cell population in a heterogeneous pool of CA TMSCs. Furthermore, assessment of the migration capacity of csGRP78+ TMSCs revealed that the csGRP78+ cells possess a higher migration speed than the unsorted and csGRP78- cells (19.63 ± 6.52 *vs.* 14.11 ± 2.29 μm/h; $p < 0.01$)

(Fig. S4d).

The differentiation efficiency of csGRP78+ cells was assessed by comparing the adipogenic, osteogenic, and chondrogenic differentiation potentials of csGRP78+ and csGRP78- cells. We found that csGRP78+ cells had higher adipogenic (2.1 ± 0.1-fold), osteogenic (6.7 ± 0.4-fold), and chondrogenic (1.2 ± 0.1-fold) differentiation potentials compared

to csGRP78- cells (Fig. 5b). The mitochondrial metabolism-related OCR values, including basal OCR (127.1 ± 31.2 to 71.5 ± 35.8 pmol/min; $p < 0.05$), proton leak (56.1 ± 16.9 to 27.9 ± 7.8 pmol/min; $p < 0.01$), non-mitochondrial oxygen consumption (94.1 ± 18.6 to 59.4 ± 11.0 pmol/min; $p < 0.01$), ATP production (71.0 ± 14.4 to 43.5 ± 12.0 pmol/min; $p < 0.01$), and SRC (886.7 ± 72.3 to 180.4 ± 37.5 pmol/min; $p < 0.01$), were significantly higher in csGRP78+ cells compared to csGRP78- cells (Fig. 5c and d). To investigate the correlation between csGRP78 and cell proliferation, the real-time proliferation rates of the control and CA TMSCs were calculated ($p < 0.001$). As shown in Fig. 5e and f, the presence of GRP78 in csGRP78+ cells significantly influenced cell proliferation compared to *GRP78* knockdown cells ($p < 0.001$). The *GRP78* knockdown using *GRP78* siRNA (siGRP78) (Fig. 5g and h) led to

the suppression of the expression of the ER stress markers, p-ATF6[Thr166] and ATF6. The p53 signaling pathway, a cellular proliferation signaling pathway, was also significantly inhibited, as indicated by the decreased levels of p-p53[Ser15]. In the AKT signaling pathway, only p-AKT[Ser473] levels were significantly decreased following siGRP78 transfection.

3.6. Embedding the TMSCs in the ROS-hydrogel

We synthesized gelatin-based *in situ* cross-linkable hydrogels (gelatin-hydroxyphenyl propionic acid, GHPA) using an HRP/H_2O_2-mediated crosslinking reaction. The incorporation of GOx into the HRP/H_2O_2 crosslinking system allowed the creation of stiff hydrogels without compromising on cytocompatibility, as GOx gradually generated H_2O_2
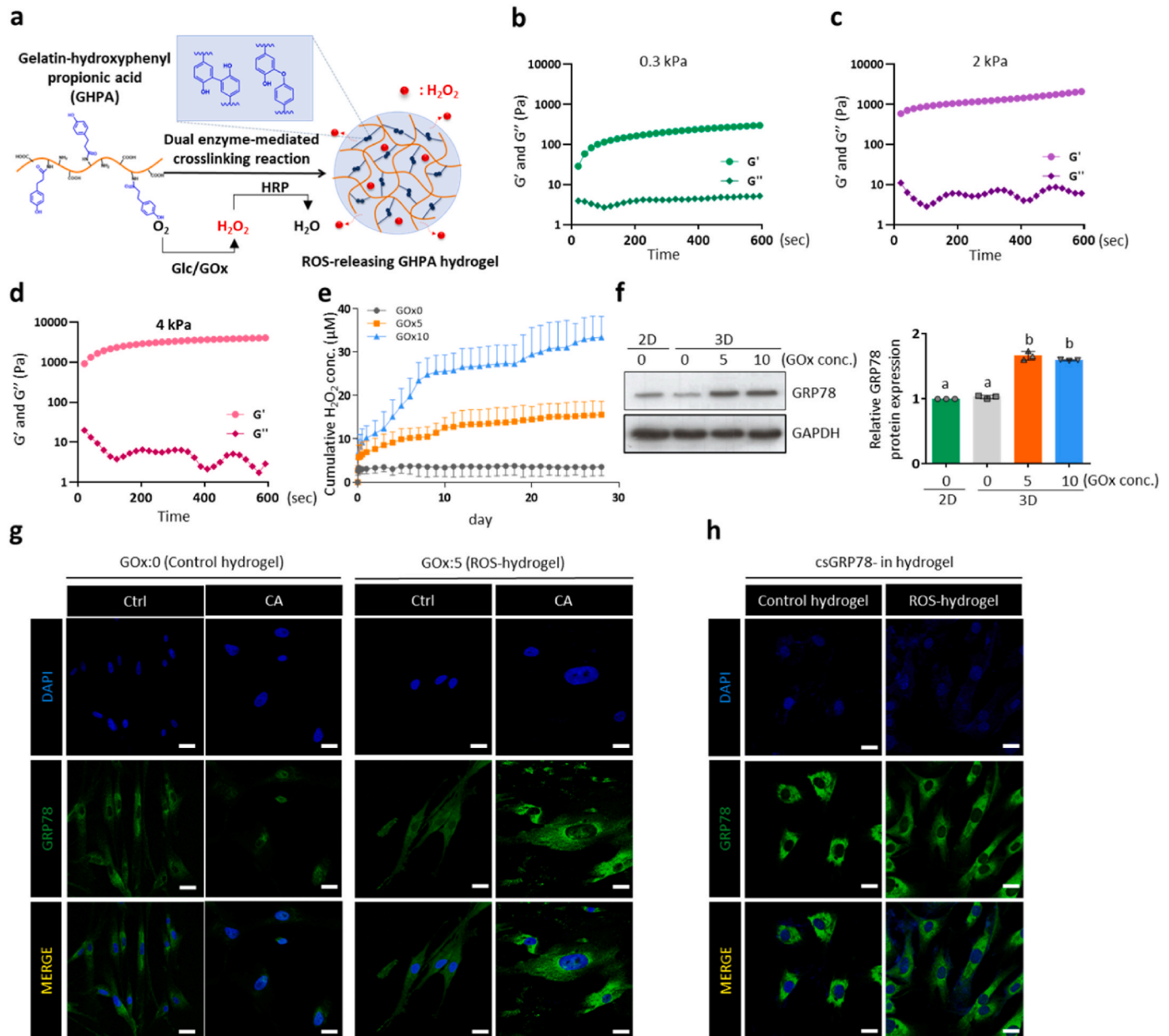

Fig. 6. Application and effects of ROS-hydrogel on the intracellular translocation of GRP78. a) Schematic illustration of the ROS-hydrogel synthetic process. The elastic modulus (G') and viscous modulus (G") of gelatin-based *in situ* cross-linkable hydrogels with different H_2O_2 concentrations: b) 0.035 wt% and 0.3 kPa, c) 0.062 wt% and 2 kPa, and d) 0.13 wt% and 4 kPa, respectively. e) Cumulative concentration of ROS released from ROS-hydrogel formulated with GOx0, GOx5, and GOx10. f) Western blot analyses of TMSCs cultured without the hydrogel (2D) and with ROS-hydrogels (3D) releasing ROS at three different levels. g) Intracellular distribution of GRP78 in TMSCs embedded in the control hydrogel and ROS-hydrogel, respectively. h) Intracellular distribution of GRP78- cells embedded in the ROS-hydrogel at GOx0 and GOx5 conditions (scale bar = 20 μm, n = 3).

during hydrogel formation.

We fabricated ROS-hydrogels through enzymatic crosslinking in the presence of HRP and H_2O_2, yielding either C–C bonds between ortho-carbons of the aromatic ring or through C–O bonds between the ortho carbon and the phenoxy oxygen (Fig. 6a) [31]. To determine the optimal stiffness of hydrogels required to provide the 3D artificial cellular microenvironment, the elastic (G′) and viscous (G″) moduli of the control hydrogels, fabricated with different H_2O_2 concentrations

(0.035–0.13 wt%), were investigated. The G′ and G″ values of the control hydrogels were measured for 10 min, when the values reached a plateau without further change. The maximum G′ values, depending on the H_2O_2 concentrations, were approximately 0.3 kPa (0.035 wt%), 2 kPa (0.062 wt%), and 4 kPa (0.13 wt%) (Fig. 6b–d). As previously described, the increase in H_2O_2 concentration with fixed HRP concentration could lead to higher crosslinking density and produce hydrogels with higher stiffness because H_2O_2 acts as a cross-linker in this system [32]. The
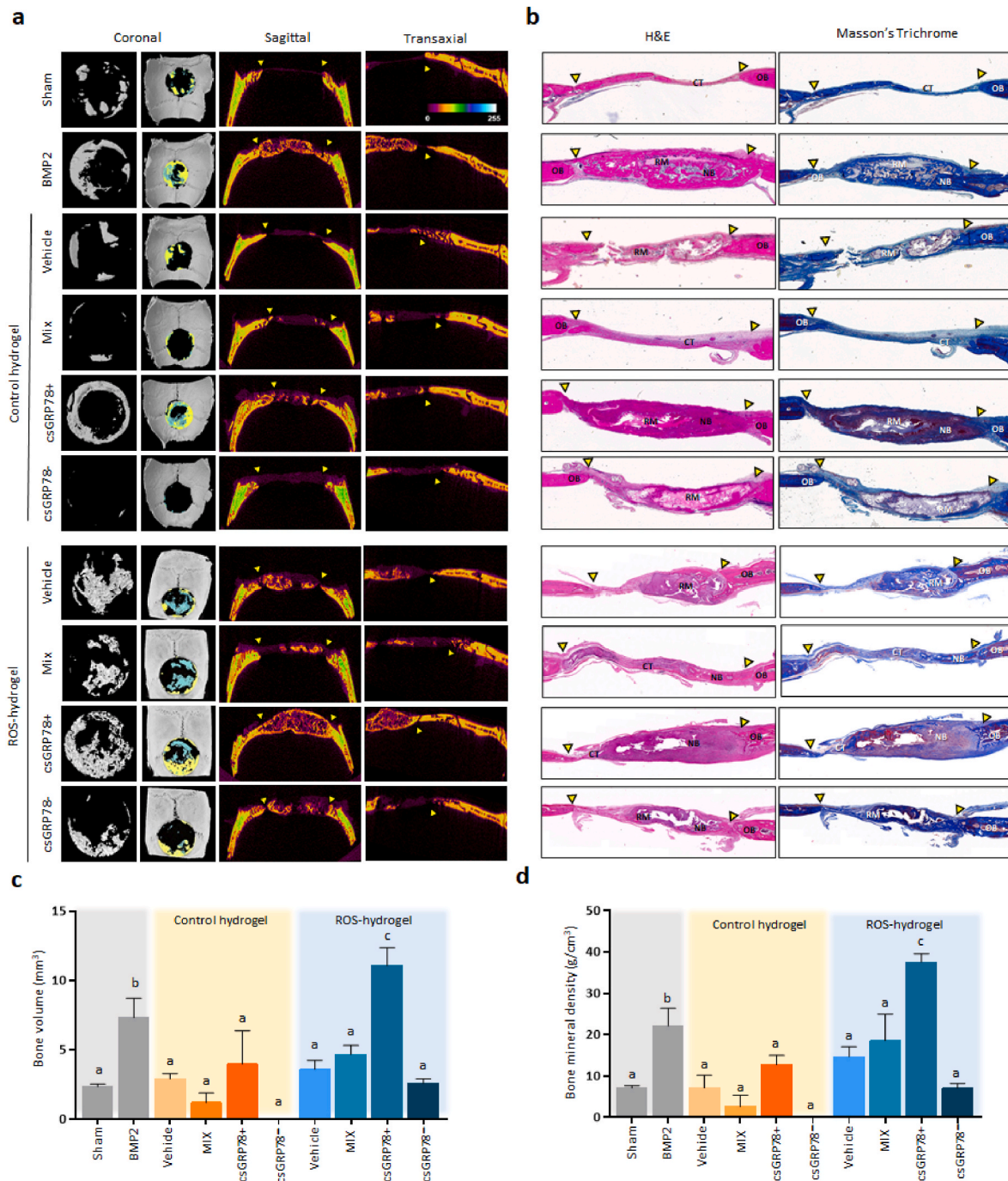

Fig. 7. Implantation efficacy of csGRP78+ cells embedded in ROS-hydrogel in a calvarial defect rat model. a) Bone regeneration was evaluated 4 weeks after implantation. Images of new bone formation in the defective area obtained using μCT. The yellow color corresponds to newly generated bone tissue, and the blue-marked area represents the fibrous connective tissue. b) Histologic sections were stained using H&E and Masson's trichrome staining methods. The yellow arrow head indicates the original defective edge; OB, NB, and RM indicate the old bone, newly formed bone, and hydrogel remnants, respectively. c, d) Morphometric analyses of the regenerated bone area are presented as bone volume (BV, mm^3) and bone mineral density (BMD, g/cm^3). The alphabets in the figure indicate the significant differences among the experimental groups ($p < 0.05$) (n = 10 rats/group). (For interpretation of the references to color in this figure legend, the reader is referred to the Web version of this article.)

cumulative H_2O_2 concentrations released from GOx0, GOx5, and GOx10 were monitored for 28 days (Fig. 6e). The cumulative maximum H_2O_2 concentrations from GOx0, GOx5, and GOx10 were 3.5 ± 0.1, 15.6 ± 0.1, and 33.3 ± 0.2 μM, respectively, with the exception of GOx10, which are considered low physiological ROS concentrations [33].

We examined the degradation and stiffness profiles of the ROS-hydrogel (GOx0, GOx5, and GOx10) at two different stiffnesses (2 and 4 kPa), with or without TMSCs, for 50 days (Figs. S5a–d). In GOx5 and GOx10 hydrogels, the mass of ROS-hydrogels embedded with TMSCs rapidly decreased at 22 and 25 days (49.5% decrease from the initial gel weight), respectively. The ROS-hydrogels without cells had a lower mass loss than those with cells throughout the experimental period. Based on these results, the optimal stiffness of the ROS-hydrogel for cell loading was achieved using GOx5 and GOx10.

To test the effect of ROS-hydrogel on GRP78 expression, control and CA TMSCs were embedded in the ROS-hydrogel (3D culture condition) with three different GOx conditions (Fig. 6f). Compared to non-embedded TMSCs (indicated as 2D), embedded 3D-cultured TMSCs presented 1.7 ± 0.1- and 1.6 ± 0.1-fold higher GRP78 expression under GOx5 and GOx10 conditions, respectively. To further optimize the biocompatibility of the ROS-hydrogel, we conducted the LIVE/DEAD assay (Figs. S5e and f), and found no significant cell death in TMSCs embedded in the GOx5 hydrogel. However, the Gox10 hydrogel exhibited a significantly higher number of dead cells compared to Gox5 hydrogel (1.7 ± 0.1-fold relative fluorescence unit (RFU); $p < 0.001$). Therefore, we selected the Gox5 and 2 kPa stiffness as optimal conditions for formulating the ROS-releasing hydrogel, denoted as "ROS-hydrogel", for further experiments with TMSCs, while the vehicle hydrogel GOx0-hydrogel is denoted as "control hydrogel". Additionally, we examined the effect of sustained ROS release on the changes in the intracellular distribution of GRP78 by loading TMSCs in either the control or ROS-hydrogel (Fig. 6g). In the case of the CA TMSCs in GOx5 ROS-hydrogel, GRP78 was mainly expressed in the plasma membrane region and cytosol, similar to the control cells. In the csGRP78- cells with GOx0 hydrogel, GRP78 was mostly distributed in the perinuclear region (left panel of Fig. 6h) of the cultured cells. Notably, GRP78- cells loaded in the GOx5 hydrogel recovered the protein expression of GRP78 evenly distributed in the cytosol (right panel of Fig. 6h). Thus, a mild ROS concentration (below the level of 4.5 μM ROS) can help the senescent cells recover GRP78 expression and enable the redistribution of intracellular GRP78 to the cell membrane and cytosol.

3.7. csGRP78+ cell-embedded ROS-hydrogel accelerates bone regeneration

To examine the tissue regeneration efficacy of csGRP78+ cells, we implanted csGRP78+ cells fabricated with the ROS-hydrogel into the calvarial defect areas of rats (Fig. 7a). Four weeks after the implantations, the morphology of the newly formed bone in the calvarial defect site was reconstructed using micro-CT (μCT), gross observation, and histological evaluation. The implantation of the control hydrogel (vehicle) without cells induced some trabecular bone formation compared to the sham group. Implantation of the control hydrogel incorporated with unsorted mixed TMSCs (Mix) did not dramatically induce bone formation compared to the hydrogel vehicle. Additionally, csGRP78- cell-loaded hydrogel implantation did not induce any new bone formation. However, compared to the other hydrogel-implanted groups, csGRP78+ cell-loaded hydrogel implantation dramatically induced the formation of new bone at the implanted defective site. ROS-hydrogel implantation resulted in more bone formation compared to the control hydrogel. As expected, csGRP78+ cell-loaded ROS-hydrogel implantation significantly improved new bone formation compared to the control hydrogel embedded with csGRP78+ cells. Unlike the control hydrogel, the ROS-hydrogel incorporated with either the Mix or csGRP78- cells induced bone formation at the implanted defect site.

Furthermore, we conducted hematoxylin and eosin (H&E) and

Masson's trichrome staining to evaluate the histology of the newly generated bone tissue (Fig. 7b, Figs. S6 and S7). Except for the sham group and the groups that were implanted with the Mix, there was showed connective tissue between the bone tissues in all groups. A thin connective tissue consisting of fibroblast-like cells was observed in the sham group and the groups implanted with the Mix without hydrogel. Histological analyses revealed that BMP2 completely recovered the defective bone region and collagenous tissue. Compared to BMP2, both hydrogels combined with csGRP78+ cells remarkably improved the generation of new bone and collagen fiber tissues. However, the implantation of csGRP78- cells using either the control hydrogel or ROS-hydrogel resulted in scaffold remnants and the formation of immature woven bone at the defective sites. Tissue staining and immunofluorescence of the retrieved samples confirmed incomplete healing in csGRP78- implanted group as the defects were primarily bridged with fibrous tissue, cartilage, and remnant. Conversely, robust bone formation was seen in the csGRP78+ implanted area, with some defects filled in completely with new bone as indicated with high cell population of $CD31^+$ cells. Trichrome staining of calvarial defect microsections harvested at 4 weeks post-treatment corroborated these findings by showing a higher proportion of mature bone and red blood cells in the csGRP78+ implanted sites than those implanted with csGRP78-. At csGRP78+ sites, no trace of ROS hydrogel was observed, suggesting complete degradation of the implanted scaffold.

Newly induced bone formation was quantified in terms of bone volume (BV, mm^3) (Fig. 7c) and bone mineral density (BMD, g/cm^3) (Fig. 7d). Both BV and BMD showed the same differences among the experimental groups. Compared to the bone morphogenetic protein 2 (BMP2) group (7.3 ± 1.1 mm^3), no significant differences were observed in the BV among the groups incorporated with the control hydrogel, even though some bone formation was present in the csGRP78+ cell-embedded group (4.3 ± 2.3 mm^3, $p > 0.05$). Hence, the incorporation of csGRP78+ cells in the ROS-hydrogel significantly improved bone formation (11.1 ± 1.3 mm^3). The csGRP78+ cell-loaded ROS-hydrogel significantly improved the BMD (37.6 ± 1.6 g/cm^3) compared to the csGRP78+ cell-loaded control hydrogel, which showed a significant recovery value (12.7 ± 1.9 g/cm^3) compared to that of the BMP2 group.

4. Discussion

The present study sought to identify a novel biomarker for isolating senescent MSCs from heterogeneous cell populations to improve stem cell therapeutic efficacy. Mounting evidence has shown the significant negative impact of replicative senescence (i.e., *in vitro* aging, also known as the Hayflick limit) on stem cell therapy [6,34,35]. In this study, we have developed a senescent TMSC model and validated its senescence characteristics by examining the changes in cell proliferation, cell cycle, metabolic rate, and differentiation efficacy.

Both transcriptomic and proteomic analyses revealed different gene expression patterns in the control and CA TMSCs (Fig. 2, Tables S1–3). Of these, we screened for molecules involved in ER stress and UPR signaling, which are essential for maintaining low levels of ROS for cell survival and differentiation. We identified GRP78 as a potential marker associated with the replicative senescence of TMSCs (Fig. 3). UPR signaling is vital for maintaining low levels of ROS and transcriptionally regulating detoxifying enzymes [36,37]. Under these conditions, cell differentiation is affected by various factors, including the duration and patterns of exposure, cellular antioxidant content, and simultaneous co-exposure to other factors [1].

GRP78 is an ER chaperone protein and gatekeeper of the mammalian UPR, which balances cell life and death by regulating the activities of ER stress sensors to sustain ER protein-folding capacity [24]. In particular, the protein level and activity of several ER chaperones including GRP78 decrease during physiological aging [28]. Under an ER stress, GRP78 dissociates from all three UPR transducers (ATF6, IRE1, and PERK), and permits stress sensors to activate downstream JNK signaling and the

eIF2α-ATF4-CHOP pathways, which trigger apoptotic cell death. ATF6 also functions as a transcription factor that induces the expression of GRP78. As replicative senescence progresses, the protein level and activity of ATF6 (as indicated by the phosphorylation of ATF6) significantly decreases (Fig. 3), consequently suppressing JNK signaling, which is vital for maintaining self-renewal and differentiation of stem cells in the CA TMSCs [38,39].

Knockdown of *GRP78* using siRNA in csGRP78+ cells significantly decreased ATF6 expression and phosphorylation, indicating a direct association between GRP78 and ATF6. ATF6 regulates the transcription of pro-survival genes such as *GRP78* [40], *GRP94*, and protein disulfide isomerases [27]. Unlike ATF6, PERK expression was not altered by siGRP78 treatment (Fig. 5). Upon siGRP78-mediated downregulation of GRP78, PERK forms a homodimer and phosphorylates eIF2α, thereby inhibiting transcription and inducing cell apoptosis [41–43]. Since we did not observe a decrease in PERK level following siGRP78 transfection, we cannot comment on the interaction between the two proteins. Collectively, we propose that GRP78 plays an important role in cell proliferation and is intricately linked to ATF6 expression and activation, among other UPR sensor proteins, under the current experimental conditions.

To further confirm the effects of csGRP78 on cell survival and proliferation, we examined the AKT and p53 signaling pathways, which play a significant role in determining cell death/survival and p53-dependent senescence [44]. As shown in Fig. 5g and h, p-p53^{Ser15} and p-AKT^{Ser473} were affected by siGRP78 transfection. p53 plays a key role in determining cell fate, and its activation takes place in a DNA damage response (DDR)-dependent or -independent manner [35,45]. p53 activation regulates metabolism, autophagy, DNA damage repair, cell cycle arrest, quiescence, senescence, and apoptosis in cancer stem cells [44]. Given the decreased *TRF-1/2* expression in senescent TMSCs and decreased p53 and AKT levels in *GRP78*-silenced csGRP78+ cells, we propose that the inhibition of GRP78 expression can affect p53 and AKT activation, thereby inducing cellular senescence and decreasing cell survival and proliferation [46].

Additionally, we found that replicative senescence dramatically altered the intracellular location of GRP78. GRP78 exclusively resides in the lumen and ER membrane [25], but it can also be secreted and actively translocated to other cellular locations, such as the cell surface, cytosol, nucleus, and mitochondria, to regulate cell signaling, proliferation, invasion, apoptosis, inflammation, and immunity [24]. Here, we observed the translocation of GRP78 from the cytoplasm and cell membrane to the (peri)nucleus in senescent TMSCs. Thus far, no direct evidence and mechanisms have explained the role of csGRP78 translocation in stem cell function and senescence. Some studies have reported the potential role of GRP78 during ER stress in human AD-MSCs and mouse neural stem cells [47,48]. Here, for the first time, we have shown the recovery of GRP78 in TMSCs exposed to ROS.

To elucidate the effect of csGRP78 on replicative senescence, we isolated csGRP78+ cells from a heterogeneous pool of TMSCs and compared their stemness with that of csGRP78- cells. The csGRP78+ cells showed significantly higher proliferation, mitochondrial metabolism, and multi-differentiation capacity than csGRP78- cells, without affecting the inherent ability of MSCs [49]. It is known that the interaction between ER and mitochondria during senescence is important. Dorian et al. (2021) reported that cellular senescence increases the mitochondria-ER contacts (MERC), brings the mitochondria and ER membranes closer, and increases ROS concentration, including Ca^{2+} ions, leading to apoptosis [50]. The efficiency of mitochondrial energy metabolism was investigated to distinguish the intracellular metabolic rate of csGRP78+ cells from mixed cells or csGRP78- cells. In this study, csGRP78+ cells had comparatively higher metabolic rates, including SRC and ATP production, which can be attributed to their relatively increased cell proliferation compared to csGRP78- cells. csGRP78+ cells also retained higher basal OCR, proton leak, non-MOC, SRC, and ATP production, indicating a potential association between the cytosolic and membrane expression of GRP78, mitochondrial function, and stemness of TMSCs.

Mitochondria and ER are the major organelles for ROS production. An appropriate level of ROS is required for cells to maintain normal physiological functions and activities [51–53]. However, ROS act as a double-edged sword in many pathophysiological conditions [54]. ROS promote growth and survival at low physiological intracellular levels (0.001–0.7 μM). However, at levels higher than 20 μM, they halt cell growth, eventually leading to cell death [14]. Here, we hypothesized that a hydrogel system that persistently releases low levels of ROS could enhance GRP78 expression in TMSCs, thereby improving their stemness and differentiation potential. Therefore, we developed a gelatin-based 3D hydrogel culture system that released a mild concentration of ROS to promote intracellular translocation and expression of GRP78. This ROS-hydrogel consistently released an appropriate concentration of H$_2$O$_2$ (5 μM) through a GOx reaction within the hydrogel.

Among the hydrogel degradation profiles obtained by using three levels of hydrogel stiffness (0.3, 2, and 4 kPa), the 0.3 kPa stiffness hydrogel was excluded due to its lack of embedded cell-holding capacity, and the 4 kPa hydrogel was excluded because it altered the original cell morphology and had an inappropriate degradation rate, resulting in hydrogel remnants at the implanted area, thereby hindering the regeneration efficacy of new tissue. We also tested various GOx conditions and found that GOx10 resulted in significant cell death (Fig. S5f). Therefore, we selected GOx5 as the optimal effective concentration of GOx for the hydrogel to restore the stemness of TMSCs (Fig. 6). When the senescent TMSCs and GRP78- cells were exposed to a mild level ROS-releasing environment (approximately 5 μM), both GRP78 expression and intracellular location were almost recovered to that in young and healthy TMSCs (Fig. 6g and h).

Finally, we evaluated the bone regeneration efficacy of the ROS-hydrogel using a calvarial defect model. We found that the ROS-hydrogel combined with csGRP78+ cells resulted in the highest bone regeneration potential compared to the other conditions tested in this study, including the Mix and csGRP78- groups (Fig. 7). Compared to the control hydrogel, without ROS release, the ROS-hydrogel presented remarkably improved new bone formation at the bone defect site. Both hydrogels resulted in significant bone regeneration capacity when implanted with csGRP78+ cells, but the csGRP78+ embedded the ROS-hydrogel showed higher bone regeneration efficacy, CD31$^+$ cell population, and collagenous tissue formation with red blood cells indicating formation of new blood vessels [55]. In contrast, the implantation of either vehicle or csGRP78- cells resulted in an apparent accumulation of hydrogel remnants at the defective site, regardless of the hydrogel type, owing to the lack of stem cell function (stemness and multi-differentiation potential) and weak proliferation capacity of csGRP78- cells, which caused the incomplete degradation of hydrogels, thereby hindering new bone formation in the defective area. Nevertheless, it remains unclear how low levels of ROS induce the stemness and regenerative capacity of TMSCs. Therefore, further studies are warranted to establish the mechanisms by which mild levels of ROS from the hydrogel induce GRP78 translocation from the nucleus to the cytoplasm and cell membrane of TMSCs.

We have demonstrated that csGRP78+ cells strongly exhibit stemness characteristics in MSCs, retaining higher proliferation and differentiation capacities compared to csGRP78- cells. Persistent exposure to mild levels of ROS through the ROS-hydrogel system further improved the regeneration capacity of csGRP78+ cells (Fig. 8). The present results indicate that csGRP78+ can be used as a potential biomarker for distinguishing senescent MSCs. Moreover, the combined use of csGRP78+ and the ROS-hydrogel system can further improve and recover the stemness of MSCs, producing high yield and high quality MSC-based therapeutic products.
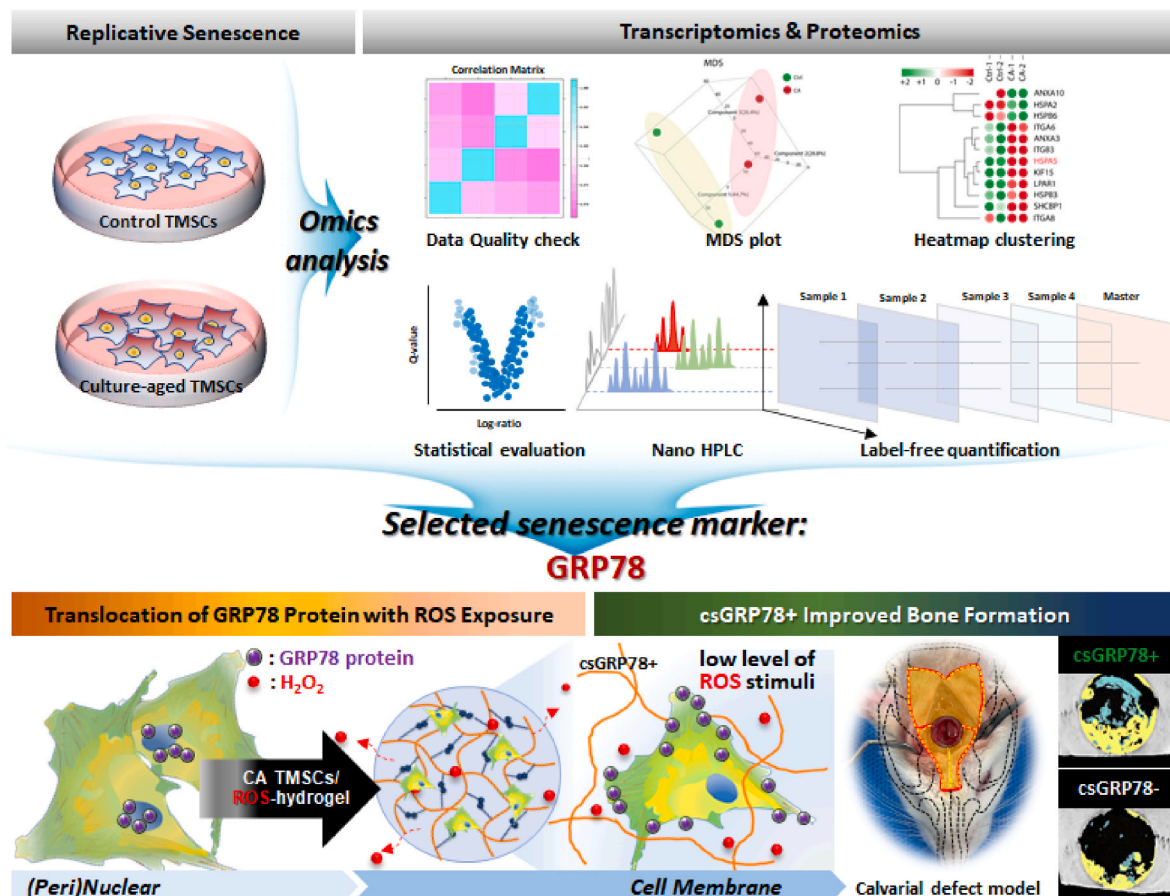
Fig. 8. An overview of the overall experimental process performed in the current study. Probe for the differentially expressed of genes and proteins among the early and late passage TMSC groups using transcriptomic and proteomic analyses revealed senescence markers, among which GRP78 was selected for use in the study.

Data availability

The raw/processed data required to reproduce these findings cannot be shared at this time as the data also forms part of an ongoing study.

Credit author statement

Yoon Shin Park, Inho Jo, Ki Dong Park, Yoon Jeong Park: Conceptualization, Da Hyeon Choi: Methodology, Software, Jue-Yeon Lee: Data curation, Da Hyeon Choi, Se-Young Oh: Writing- Original draft preparation, Kyeong Eun Lee, Si Min Lee, Jong-Chul Park, Beom Soo Jo: Visualization, Investigation, Yoon Shin Park: Supervision, Writing-Reviewing and Editing.

Declaration of competing interest

The authors declare the following financial interests/personal relationships which may be considered as potential competing interests: Yoon Shin Park has patent #PF-B2389-US pending to U.S.Department of Commerce.

Acknowledgements

Appendix A. Supplementary data

Supplementary data to this article can be found online at https://doi.org/10.1016/j.biomaterials.2021.121156.

References

[1] T. Kamiya, M. Courtney, M.O. Laukkanen, Redox-activated signal transduction pathways mediating cellular functions in inflammation, differentiation, degeneration, transformation, and death, Oxid. Med. Cell. Longev. (2016) 8479718, 2016.

[2] S.Y. Oh, Y.M. Choi, H.Y. Kim, Y.S. Park, S.C. Jung, J.W. Park, S.Y. Woo, K.H. Ryu, H.S. Kim, I. Jo, Application of tonsil-derived mesenchymal stem cells in tissue regeneration: concise review, Stem Cell. 37 (10) (2019) 1252–1260.

[3] R. Liang, S. Ghaffari, Stem cells, redox signaling, and stem cell aging, Antioxidants Redox Signal. 20 (12) (2014) 1902–1916.

[4] S.R. Yang, J.R. Park, K.S. Kang, Reactive oxygen species in mesenchymal stem cell aging: implication to lung diseases, Oxid. Med. Cell. Longev. (2015) 486263, 2015.

[5] S. Neri, R.M. Borzi, Molecular mechanisms contributing to mesenchymal stromal cell aging, Biomolecules 10 (2) (2020).

[6] J. Neves, P. Sousa-Victor, H. Jasper, Rejuvenating strategies for stem cell-based therapies in aging, Cell Stem Cell 20 (2) (2017) 161–175.

[7] W. Wagner, P. Horn, M. Castoldi, A. Diehlmann, S. Bork, R. Saffrich, V. Benes, J. Blake, S. Pfister, V. Eckstein, A.D. Ho, Replicative senescence of mesenchymal stem cells: a continuous and organized process, PloS One 3 (5) (2008), e2213.

[8] G. Kim, Y.M. Jin, Y. Yu, H.Y. Kim, S.A. Jo, Y.J. Park, Y.S. Park, I. Jo, Double intratibial injection of human tonsil-derived mesenchymal stromal cells recovers postmenopausal osteoporotic bone mass, Cytotherapy 20 (8) (2018) 1013–1027.

[9] M. Yoo, S. Cho, S. Shin, J. Kim, H. Park, S. Cho, Y.K. Hwang, D.H. Park, Therapeutic effect of IL1β priming tonsil derived-mesenchymal stem cells in osteoporosis, Tissue. Eng. Regen. Med. 18 (5) (2021) 851–862.

[10] H.S. Park, J. Lee, J.W. Kim, H.Y. Kim, S.Y. Jung, S.M. Lee, C.H. Park, H.S. Kim, Preventive effects of tonsil-derived mesenchymal stem cells on osteoradionecrosis in a rat model, Head Neck 40 (3) (2018) 526–535.

[11] S.J. Lee, J.E. Won, C. Han, X.Y. Yin, H.K. Kim, H. Nah, I.K. Kwon, B.H. Min, C. H. Kim, Y.S. Shin, S.A. Park, Development of a three-dimensionally printed scaffold

grafted with bone forming peptide-1 for enhanced bone regeneration with in vitro and in vivo evaluations, J. Colloid Interface Sci. 539 (2019) 468–480.

[12] P.V. Luoma, Elimination of endoplasmic reticulum stress and cardiovascular, type 2 diabetic, and other metabolic diseases, Ann. Med. 45 (2) (2013) 194–202.

[13] A. Nugud, D. Sandeep, A.T. El-Serafi, Two faces of the coin: minireview for dissecting the role of reactive oxygen species in stem cell potency and lineage commitment, J. Adv. Res. 14 (2018) 73–79.

[14] R. Mittler, ROS are good, Trends Plant Sci. 22 (1) (2017) 11–19.

[15] D. Zhou, L. Shao, D.R. Spitz, Reactive oxygen species in normal and tumor stem cells, Adv. Canc. Res. 122 (2014) 1–67.

[16] Y.Y. Jang, S.J. Sharkis, A low level of reactive oxygen species selects for primitive hematopoietic stem cells that may reside in the low-oxygenic niche, Blood 110 (8) (2007) 3056–3063.

[17] A. Cieslar-Pobuda, J. Yue, H.C. Lee, M. Skonieczna, Y.H. Wei, ROS and oxidative stress in stem cells, Oxid. Med. Cell. Longev. (2017) 5047168, 2017.

[18] J. Wang, W. He, P.J. Tsai, P.H. Chen, M. Ye, J. Guo, Z. Su, Mutual interaction between endoplasmic reticulum and mitochondria in nonalcoholic fatty liver disease, Lipids Health Dis. 19 (1) (2020) 72.

[19] O. Pluquet, A. Pourtier, C. Abbadie, The unfolded protein response and cellular senescence. A review in the theme: cellular mechanisms of endoplasmic reticulum stress signaling in health and disease, Am. J. Physiol. Cell Physiol. 308 (6) (2015) C415–C425.

[20] H.M. Zeeshan, G.H. Lee, H.R. Kim, H.J. Chae, Endoplasmic reticulum stress and associated ROS, Int. J. Mol. Sci. 17 (3) (2016) 327.

[21] M. Farshbaf, A.Y. Khosroushahi, S. Mojarad-Jabali, A. Zarebkohan, H. Valizadeh, P.R. Walker, Cell surface GRP78: an emerging imaging marker and therapeutic target for cancer, J. Contr. Release 328 (2020) 932–941.

[22] S.V. Pizzo, Cell Surface GRP78, a New Paradigm in Signal Transduction Biology, 2018.

[23] J. Mao, Y. Hu, L. Ruan, Y. Ji, Z. Lou, Role of endoplasmic reticulum stress in depression (Review), Mol. Med. Rep. 20 (6) (2019) 4774–4780.

[24] M. Ni, Y. Zhang, A.S. Lee, Beyond the endoplasmic reticulum: atypical GRP78 in cell viability, signalling and therapeutic targeting, Biochem. J. 434 (2) (2011) 181–188.

[25] S. Vig, M. Buitinga, D. Rondas, I. Crevecoeur, M. van Zandvoort, E. Waelkens, D. L. Eizirik, C. Gysemans, P. Baatsen, C. Mathieu, L. Overbergh, Cytokine-induced translocation of GRP78 to the plasma membrane triggers a pro-apoptotic feedback loop in pancreatic beta cells, Cell, Death. Dis. 10 (4) (2019) 309.

[26] L. Sisinni, M. Pietrafesa, S. Lepore, F. Maddalena, V. Condelli, F. Esposito, M. Landriscina, Endoplasmic reticulum stress and unfolded protein response in breast cancer: the balance between apoptosis and autophagy and its role in drug resistance, Int. J. Mol. Sci. 20 (4) (2019).

[27] Q.J. Quinones, G.G. de Ridder, S.V. Pizzo, GRP78: a chaperone with diverse roles beyond the endoplasmic reticulum, Histol. Histopathol. 23 (11) (2008) 1409–1416.

[28] K.T. Pfaffenbach, A.S. Lee, The critical role of GRP78 in physiologic and pathologic stress, Curr. Opin. Cell Biol. 23 (2) (2011) 150–156.

[29] B.Y. Kim, Y. Lee, J.Y. Son, K.M. Park, K.D. Park, Dual enzyme-triggered in situ crosslinkable gelatin hydrogels for artificial cellular microenvironments, Macromol. Biosci. 16 (11) (2016) 1570–1576.

[30] D.H. Choi, S.Y. Oh, J.K. Choi, K.E. Lee, J.Y. Lee, Y.J. Park, I. Jo, Y.S. Park, A transcriptomic analysis of serial-cultured, tonsil-derived mesenchymal stem cells reveals decreased integrin alpha3 protein as a potential biomarker of senescent cells, Stem Cell Res. Ther. 11 (1) (2020) 359.

[31] Y. Lee, J.W. Bae, D.H. Oh, K.M. Park, Y.W. Chun, H.J. Sung, K.D. Park, In situ forming gelatin-based tissue adhesives and their phenolic content-driven properties, J. Mater. Chem. B. 1 (18) (2013) 2407–2414.

[32] K.M. Park, Y.M. Shin, Y.K. Joung, H. Shin, K.D. Park, In situ forming hydrogels based on tyramine conjugated 4-Arm-PPO-PEO via enzymatic oxidative reaction, Biomacromolecules 11 (3) (2010) 706–712.

[33] Y. Lee, J.Y. Son, J.I. Kang, K.M. Park, K.D. Park, Hydrogen peroxide-releasing hydrogels for enhanced endothelial cell activities and neovascularization, ACS Appl. Mater. Interfaces 10 (21) (2018) 18372–18379.

[34] G. de Haan, S.S. Lazare, Aging of hematopoietic stem cells, Blood 131 (5) (2018) 479–487.

[35] A. Lujambio, To clear, or not to clear (senescent cells)? That is the question, Bioessays 38 (Suppl 1) (2016) S56–S64.

[36] T. Avril, E. Vauleon, E. Chevet, Endoplasmic reticulum stress signaling and chemotherapy resistance in solid cancers, Oncogenesis 6 (8) (2017) e373.

[37] H. Urra, E. Dufey, T. Avril, E. Chevet, C. Hetz, Endoplasmic reticulum stress and the hallmarks of cancer, Trends Cancer 2 (5) (2016) 252–262.

[38] T. Semba, R. Sammons, X. Wang, X. Xie, K.N. Dalby, N.T. Ueno, JNK signaling in stem cell self-renewal and differentiation, Int. J. Mol. Sci. 21 (7) (2020).

[39] W. Rozpedek, D. Pytel, B. Mucha, H. Leszczynska, J.A. Diehl, I. Majsterek, The role of the PERK/eIF2alpha/ATF4/CHOP signaling pathway in tumor progression during endoplasmic reticulum stress, Curr. Mol. Med. 16 (6) (2016) 533–544.

[40] Y.J. Chern, J.C.T. Wong, G.S.W. Cheng, A. Yu, Y. Yin, D.F. Schaeffer, H. F. Kennecke, G. Morin, I.T. Tai, The interaction between SPARC and GRP78 interferes with ER stress signaling and potentiates apoptosis via PERK/eIF2alpha and IRE1alpha/XBP-1 in colorectal cancer, Cell Death Dis. 10 (7) (2019) 504.

[41] C. Roller, D. Maddalo, The molecular chaperone GRP78/BiP in the development of chemoresistance: mechanism and possible treatment, Front. Pharmacol. 4 (2013) 10.

[42] H. Li, C. Yang, Y. Shi, L. Zhao, Exosomes derived from siRNA against GRP78 modified bone-marrow-derived mesenchymal stem cells suppress Sorafenib resistance in hepatocellular carcinoma, J. Nanobiotechnol. 16 (1) (2018) 103.

[43] T. Suzuki, J. Lu, M. Zahed, K. Kita, N. Suzuki, Reduction of GRP78 expression with siRNA activates unfolded protein response leading to apoptosis in HeLa cells, Arch. Biochem. Biophys. 468 (1) (2007) 1–14.

[44] K.H. Vousden, C. Prives, Blinded by the light: the growing complexity of p53, Cell 137 (3) (2009) 413–431.

[45] J.M. Valentine, S. Kumar, A. Moumen, A p53-independent role for the MDM2 antagonist Nutlin-3 in DNA damage response initiation, BMC Canc. 11 (2011) 79.

[46] J. Lin, P. Countryman, N. Buncher, P. Kaur, L.E.Y. Zhang, G. Gibson, C. You, S. C. Watkins, J. Piehler, P.L. Opresko, N.M. Kad, H. Wang, TRF1 and TRF2 use different mechanisms to find telomeric DNA but share a novel mechanism to search for protein partners at telomeres, Nucleic Acids Res. 42 (4) (2014) 2493–2504.

[47] Q. Liu, Y. Li, L. Zhou, Y. Li, P. Xu, X. Liu, Q. Lv, J. Li, H. Guo, H. Cai, R. Sun, X. Liu, GRP78 promotes neural stem cell antiapoptosis and survival in response to oxygen-glucose deprivation (OGD)/Reoxygenation through PI3K/akt, ERK1/2, and NF-kappaB/p65 pathways, Oxid. Med. Cell. Longev. (2018) 3541807, 2018.

[48] Q. Yin, N. Xu, D. Xu, M. Dong, X. Shi, Y. Wang, Z. Hao, S. Zhu, D. Zhao, H. Jin, W. Liu, Comparison of senescence-related changes between three- and two-dimensional cultured adipose-derived mesenchymal stem cells, Stem Cell Res. Ther. 11 (1) (2020) 226.

[49] A. Merkel, Y. Chen, A. George, Endocytic trafficking of DMP1 and GRP78 complex facilitates osteogenic differentiation of human periodontal ligament stem cells, Front. Physiol. 10 (2019) 1175.

[50] D.V. Ziegler, D. Vindrieux, D. Goehrig, S. Jaber, G. Collin, A. Griveau, C. Wiel, N. Bendridi, S. Djebali, V. Farfariello, N. Prevarskaya, L. Payen, J. Marvel, S. Aubert, J.M. Flaman, J. Rieusset, N. Martin, D. Bernard, Calcium channel ITPR2 and mitochondria-ER contacts promote cellular senescence and aging, Nat. Commun. 12 (1) (2021) 720.

[51] J. Chapman, E. Fielder, J.F. Passos, Mitochondrial dysfunction and cell senescence: deciphering a complex relationship, FEBS Lett. 593 (13) (2019) 1566–1579.

[52] L.A. Sena, N.S. Chandel, Physiological roles of mitochondrial reactive oxygen species, Mol. Cell. 48 (2) (2012) 158–167.

[53] J. Roy, J.M. Galano, T. Durand, J.Y. Le Guennec, J.C. Lee, Physiological role of reactive oxygen species as promoters of natural defenses, Faseb. J. 31 (9) (2017) 3729–3745.

[54] X. Wang, C.X. Hai, ROS acts as a double-edged sword in the pathogenesis of type 2 diabetes mellitus: is Nrf2 a potential target for the treatment? Mini Rev. Med. Chem. 11 (12) (2011) 1082–1092.

[55] J. Han, U.H. Ko, H.J. Kim, S. Kim, J.S. Jeon, J.H. Shin, Electrospun microvasculature for rapid vascular network restoration, Tissue. Eng. Regen. Med. 18 (1) (2021) 89–97.